


# Phonon dichroism in proximitized graphene

Wen-Yu Shan(单文语)
**Citation:**Chin. Phys. B, 2023, 32 (**10**): 106301. DOI: 10.1088/1674-1056/acf207

Journal homepage: http://cpb.iphy.ac.cn; http://iopscience.iop.org/cpb

**What follows is a list of articles you may be interested in**

---

## Reduction of interfacial thermal resistance of overlapped graphene by bonding carbon chains

Yuwen Huang(黄钰文), Wentao Feng(冯文韬), Xiaoxiang Yu(余晓翔), Chengcheng Deng(邓程程), and Nuo Yang(杨诺)
Chin. Phys. B, 2020, 29 (**12**): 126303. DOI: 10.1088/1674-1056/abc677

## Multilayer graphene refractive index tuning by optical power

Lijun Li(李丽君), Yilin Liu(刘仪琳), Yinming Liu(刘荫明), Lin Xu(徐琳), Fei Yu(于飞), Tianzong Xu(徐天纵), Zhihui Shi(石志辉), Weikang Jia(贾伟康)
Chin. Phys. B, 2018, 27 (**12**): 126304. DOI: 10.1088/1674-1056/27/12/126304

## The superconducting properties of a Pb/$MoTe_2$/Pb heterostructure:First-principles calculations within the anisotropic Migdal-Eliashberg theory

Wei Xia(夏威), Jie Zhang(张洁), Gui-Qin Huang(黄桂芹)
Chin. Phys. B, 2018, 27 (**12**): 126302. DOI: 10.1088/1674-1056/27/12/126302

## Thermal transport in semiconductor nanostructures, graphene, and related two-dimensional materials

Alexandr I. Cocemasov, Calina I. Isacova, Denis L. Nika
Chin. Phys. B, 2018, 27 (**5**): 056301. DOI: 10.1088/1674-1056/27/5/056301

## Lattice vibration and thermodynamical properties of a single-layergraphene in the presence of vacancy defects

Sha Li(黎莎), Zeng-Tao Lv(吕增涛)
Chin. Phys. B, 2017, 26 (**3**): 036303. DOI: 10.1088/1674-1056/26/3/036303

---

**RAPID COMMUNICATION**

# Phonon dichroism in proximitized graphene

Wen-Yu Shan(单文语)[†]

*Department of Physics, School of Physics and Materials Science, Guangzhou University, Guangzhou* 510006, *China*

(Received 6 June 2023; revised manuscript received 6 August 2023; accepted manuscript online 21 August 2023)

We systematically investigate the phonon dichroism in proximitized graphene with broken time-reversal symmetry. We find that in the absence of any type of spin–orbit coupling, phonon dichroism vanishes. Linear and circular phonon dichroism occur in the presence of uniform (staggered) intrinsic spin–orbit coupling and ferromagnetic (antiferromagnetic) exchange coupling. All these situations can be distinguished by their specific behaviors of phonon absorption at the transition point. Our finding provides new possibilities to use phonon dichroism to identify the form of spin–orbit coupling and exchange coupling in proximitized graphene on various magnetic substrates.

**Keywords:** phonon dichroism, spin–orbit coupling, proximitized graphene, electron–phonon interaction

**PACS:** 63.22.Rc, 71.70.Ej, 63.20.kd, 73.43.–f **DOI:** 10.1088/1674-1056/acf207

## 1. Introduction

Recent years have witnessed a surge of interest in studying topological states in two-dimensional materials,[1] such as quantum anomalous Hall effect[2] and quantum spin Hall effect in graphene.[3,4] Since the occurrence of these topological states does not rely on the existence of strong magnetic field as in quantum Hall effect, they provide potential applications in dissipationless electronics and spintronics.

To realize these states, large spin–orbit coupling (SOC) or external magnetization is usually required. However, in pristine graphene, the intrinsic SOC is very weak, yielding a spin–orbit splitting $\sim$ μeV,[5,6] which is unable to drive a topological phase transition. When placing graphene on transition-metal dichalcogenides, e.g., $MoS_2$ or $WS_2$, the spin–orbit splitting can be largely enhanced up to the meV scale.[7–18] The form of SOC, according to the original proposal by Kane and Mele,[4] is uniform on A and B sublattices of graphene. However, recent spin relaxation anisotropy experiments[19–21] suggest that in heterostructures of graphene and transition metal dichalcogenides, the SOC exhibits a staggered form with opposite signs on A and B sublattices. Such a new form of SOC is proposed to support topologically protected pseudo-helical edge states in $Z_2$-trivial proximitized graphene.[22,23]

On the other hand, magnetization can be introduced in graphene by proximity to magnetic substrates with uniform (ferromagnetic) exchange coupling.[24–34] A natural question is whether these topological effects can arise from the staggered (antiferromagnetic) exchange coupling, in which case the average magnetization vanishes. Up to now, this question has received rare attention[23,38,39] since it is difficult to realize the Néel-order antiferromagnetism (AFM) in monolayer graphene. An earlier proposal is to place the graphene on an antiferromagnetic, perovskite $BiFeO_3$,[38] which, however, leads to ferromagnetic exchange in graphene. Fortunately, recent first-principles calculations[23,39–41] suggest that graphene on an Ising AFM $MnPSe_3$[42,43] would be a realistic platform for the staggered exchange coupling. This provides opportunities to investigate new physics in graphene with proximitized AFM.

Similar to electrons, phonons in topological materials may bring rich physics due to the coupling between electrons and phonons. Through the electron–phonon coupling, the topological or geometric information of electrons can be inherited by phonons, giving rise to unusual phononic behaviors, e.g., phonon Hall viscosity,[44] anomalous phonon magnetic moment,[45–49] phonon magnetochiral effect,[50,51] etc. Particularly, when left- or right-handed circularly polarized phonons are propagating in conducting materials, they may be absorbed differently by electrons, a phenomenon named circular phonon dichroism (CPD).[52] Such phenomenon can be regarded as a phononic version of Hall absorption, which requires a breaking of time-reversal symmetry by external magnetic field or magnetization. Up to now, CPD has only been theoretically studied in Weyl semimetals[52] and monolayer transition metal dichalcogenides $MoTe_2$.[53] For $MoTe_2$, ferromagnetic substrate EuO is adopted, which introduces uniform ferromagnetic exchange and a mixture of uniform and staggered SOC in the system. Nevertheless, the individual roles of uniform and staggered SOC in CPD are unclear. Moreover, when replacing the substrate EuO with AFM $MnPSe_3$, will CPD effect still survive? What are the roles of uniform and staggered SOC in that case? These issues are worth further investigation to understand better how the topology affects the phonon physics.

In this work, we study the linear and circular phonon

[†]Corresponding author. E-mail: wyshan@gzhu.edu.cn

© 2023 Chinese Physical Society and IOP Publishing Ltd 

dichroism in proximitized graphene with a combination of uniform (staggered) intrinsic SOC and ferromagnetic (antiferromagnetic) exchange coupling. We find that in each of these situations phonon dichroism can occur with unique features, particularly at the transition points. These phenomena help us better understand the phonon dynamics in proximitized antiferromagnetic graphene on the $MnPSe_3$ substrate, and provide opportunities to use phonon dichroism to identify the dominant mechanisms of SOC and exchange coupling in realistic proximitized graphene.

This paper is organized as follows. In Section 2, we introduce model and methods. The results of phonon dichroism for proximitized graphene are given in Section 3, including ferromagnetic and antiferromagnetic exchange couplings. Finally, conclusions and discussions are made in Section 4.

## 2. Model and methods

We start with the effective model of proximity modified graphene in the vicinity of Dirac points ($\pm K$ valley) $H_{\rm e}(\boldsymbol{k}) = H_0 + H_{\rm I} + H_{\rm R} + H_{\rm Z}$, where the nearest-neighbor hopping and staggered potential read

$$H_0 = \hbar v_{\rm F}(\eta k_x \sigma_x + k_y \sigma_y) s_0 + \Delta \sigma_z s_0. \tag{1}$$

Here $\sigma_i$ acts on sublattice (A, B) and $s_i$ acts on spin ($\uparrow, \downarrow$), with $i = 0, x, y, z$. $v_{\rm F}$ is the Fermi velocity and $k_{x,y}$ are wave vectors. Staggered potential $\Delta$ breaks the inversion symmetry between sublattices A and B, which opens the band gap of Dirac cones. The valley index $\eta = \pm 1$ for $\pm K$. The intrinsic SOC is given by $H_{\rm I} = H_{\rm UI} = \eta \lambda_{\rm U} \sigma_0 s_z$ or $H_{\rm I} = H_{\rm SI} = \eta \lambda_{\rm S} \sigma_z s_z$, which corresponds to the uniform and staggered intrinsic SOC, respectively. The intrinsic SOC preserves the mirror symmetry along $z$ axis, whereas the Rashba SOC $H_{\rm R} = \frac{\lambda_{\rm R}}{2}(\eta \sigma_x s_y - \sigma_y s_x)$ breaks the mirror symmetry and mixes spin $\uparrow$ and $\downarrow$. These terms constitute the experimentally relevant model for nonmagnetic proximitized graphene.[8,22,54,55] In the presence of magnetic substrates with out-of-plane magnetization, the Zeeman term is given by $H_{\rm Z} = m_{\rm F} \sigma_0 s_z$ for ferromagnetic exchange coupling, whereas $H_{\rm Z} = m_{\rm A} \sigma_z s_z$ for AFM exchange coupling.

When phonons are propagating in the graphene plane, they can be absorbed by electrons through the electron–phonon coupling $H_{\rm e-ph} = \boldsymbol{u}(\boldsymbol{q}) \cdot \boldsymbol{T}(\boldsymbol{q})$. Here $\boldsymbol{u}(\boldsymbol{q}) = (u_x, u_y)$ is the displacement of ions in the momentum space and $\boldsymbol{T}(\boldsymbol{q})$ is the effective force exerted by electrons. We mainly focus on the long-wavelength acoustic phonons, which, at each valley, have the form[56,57] $\boldsymbol{T}^{\eta=-1}(\boldsymbol{q}) = {\rm i} g[\boldsymbol{q} \cdot \boldsymbol{\sigma}, (\boldsymbol{q} \times \boldsymbol{\sigma})_z]$ and $\boldsymbol{T}^{\eta=1}(\boldsymbol{q}) = \mathcal{K}[\boldsymbol{T}^{\eta=-1}(-\boldsymbol{q})]$. $\mathcal{K}$ is the complex conjugation operator. Flexural modes, which correspond to the out-of-plane displacement, are neglected due to the weak electron–phonon coupling[58] and strong suppression by the substrates.[59–61]

The absorption coefficients are given by $\gamma_{\alpha\beta}(\boldsymbol{q}, \omega) = \sum_{\eta=\pm 1} \gamma^{\eta}_{\alpha\beta}(\boldsymbol{q}, \omega)$, $\alpha, \beta = x, y$, where the valley-resolved coefficients read[52,53]

$$\gamma^{\eta}_{\alpha\beta}(\boldsymbol{q}, \omega) = \frac{\pi}{2\omega} \sum_{n,m} \int \frac{\hbar {\rm d}^2 \boldsymbol{k}}{\rho (2\pi)^2} F^{\eta}_{mn}(\boldsymbol{k}, \boldsymbol{q}) [T^{\eta}_{\alpha}]^{mn}_{\boldsymbol{k}, \boldsymbol{k}-\boldsymbol{q}} [[T^{\eta}_{\beta}]^{mn}_{\boldsymbol{k}, \boldsymbol{k}-\boldsymbol{q}}]^*. \tag{2}$$

Here $\rho$ is the mass density of graphene and $m, n$ are the band indices. The transition matrix element $[T^{\eta}_{\alpha}]^{mn}_{\boldsymbol{k}, \boldsymbol{k}-\boldsymbol{q}} = \langle \eta, m, \boldsymbol{k} | T^{\eta}_{\alpha}(\boldsymbol{q}) | \eta, n, \boldsymbol{k} - \boldsymbol{q} \rangle$ and the dynamical factor $F^{\eta}_{mn}(\boldsymbol{k}, \boldsymbol{q}) = [f(E_{\eta,m,\boldsymbol{k}}) - f(\omega + E_{\eta,m,\boldsymbol{k}})] \delta(\omega + E_{\eta,m,\boldsymbol{k}} - E_{\eta,n,\boldsymbol{k}-\boldsymbol{q}})$. $\omega$ is the phonon energy and $E_{\eta,m,\boldsymbol{k}}$ is the eigendispersion of electronic Hamiltonian $H_{\rm e}(\boldsymbol{k})$. $f(E_{\eta,m,\boldsymbol{k}})$ is the Fermi distribution function. For long-wavelength acoustic phonons, $\omega \ll |E_{\rm F}|$ ($E_{\rm F}$ is the Fermi energy), and in the low-temperature limit,[53]

$$F^{\eta}_{nn}(\boldsymbol{k}, \boldsymbol{q}) \approx \omega \delta(E_{\eta,n,\boldsymbol{k}} - E_{\rm F}) \delta(\omega + E_{\eta,n,\boldsymbol{k}} - E_{\eta,n,\boldsymbol{k}-\boldsymbol{q}}), \tag{3}$$

where we only need to consider the intraband transition of electrons, i.e., $m = n$. For convenience, the $\gamma$ matrix can be rewritten as

$$\gamma(\boldsymbol{q}, \omega) = \begin{bmatrix} \gamma_D(\boldsymbol{q}, \omega) + \gamma_{\bar{D}}(\boldsymbol{q}, \omega) & \gamma_{\bar{A}}(\boldsymbol{q}, \omega) + {\rm i}\gamma_A(\boldsymbol{q}, \omega) \\ \gamma_{\bar{A}}(\boldsymbol{q}, \omega) - {\rm i}\gamma_A(\boldsymbol{q}, \omega) & \gamma_D(\boldsymbol{q}, \omega) - \gamma_{\bar{D}}(\boldsymbol{q}, \omega) \end{bmatrix}, \tag{4}$$

where $\gamma_D$ ($\gamma_{\bar{D}}$) refers to the symmetric (anti-symmetric) longitudinal absorption of phonons, and $\gamma_A$ ($\gamma_{\bar{A}}$) refers to the symmetric (anti-symmetric) transverse absorption. When linearly polarized longitudinal or transverse phonons are considered, that is, $|u_{\rm l}(\boldsymbol{q})\rangle = [\cos\phi_{\boldsymbol{q}}, \sin\phi_{\boldsymbol{q}}]^{\rm T}$ and $|u_{\rm t}(\boldsymbol{q})\rangle = [-\sin\phi_{\boldsymbol{q}}, \cos\phi_{\boldsymbol{q}}]^{\rm T}$, the absorption coefficients follow $\gamma^{\rm l/t} = \gamma_D \pm \cos 2\phi_{\boldsymbol{q}} \gamma_{\bar{D}} \pm \sin 2\phi_{\boldsymbol{q}} \gamma_{\bar{A}}$. $\phi_{\boldsymbol{q}}$ is the azimuthal angle of $\boldsymbol{q}$. This means that nonzero $\gamma_{\bar{D}}$ or $\gamma_{\bar{A}}$ defines the linear phonon dichroism. On the other hand, when circular phonons are injected, i.e., $|u_{\rm L/R}(\boldsymbol{q})\rangle = \frac{1}{\sqrt{2}}[1, \pm {\rm i}]^{\rm T}$, the absorption coefficients read $\gamma^{\rm L/R} = \gamma_D \mp \gamma_A$. This suggests that nonzero $\gamma_A$ defines the circular phonon dichroism. These absorption coefficients can be evaluated numerically (see Appendix A).

## 3. Results

### 3.1. Ferromagnetic exchange coupling

In this section, we show numerical results of phonon dichroism in graphene with ferromagnetic exchange coupling ($m_{\rm F} \neq 0$). For simplicity, we first consider the case without intrinsic SOC, that is, $\lambda_{\rm U} = \lambda_{\rm S} = 0$. If Rashba SOC is also absent, i.e., $\lambda_{\rm R} = 0$, we find that $\gamma_A = 0$ due to the opposite contributions from valley $\pm K$. This means that circular phonon dichroism vanishes although time-reversal symmetry is broken by ferromagnetic order.

When the Rashba SOC is present, i.e., $\lambda_R \neq 0$, numerical results are plotted in Fig. 1. According to Fig. 1(a), band dispersions at valley $\pm K$ are asymmetric, suggesting that $\gamma_A$ is non-vanishing. The Fermi level is assumed to be in the conduction band, and $k_F$ is the Fermi wave vector at valley $K$. Phonons are assumed to propagate along the $x$ direction, $\boldsymbol{q} = q_x\hat{x}$, and $\gamma_{D/\bar{D}/A}$ as functions of phonon wave vector $q_x$ are shown in Figs. 1(b)–1(d). Here $\gamma_{\bar{A}} = 0$ since $\gamma_{\bar{A}}$ is proportional to $\sin 4\phi_{\boldsymbol{q}}$,[53] where $\phi_{\boldsymbol{q}} = 0$ is the azimuthal angle of $\boldsymbol{q}$. Results for single valley $K$, $-K$ and both valleys are plotted in green, blue and yellow, respectively. We can see that there are two peaks for $\gamma_{D/\bar{D}/A}$, labeled by $q_{c1}$ and $q_{c2}$. The occurrence of peak values is because $\gamma_{D/\bar{D}/A} \propto 1/\sin\theta$ (see Appendix A) and $\theta \approx 0$ at $q = q_{c1}$ or $q_{c2}$. Here $\theta$ is the angle between the phonon wave vector $\boldsymbol{q}$ and electron wave vector $\boldsymbol{k}$, and $\boldsymbol{q} \approx 2\boldsymbol{k}$ at $q = q_{c1}$ or $q_{c2}$.

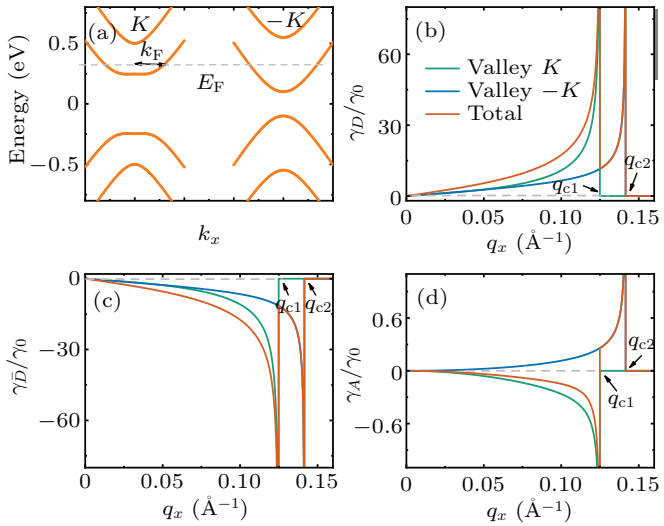



**Fig. 1.** (a) Electronic band structure and (b)–(d) phonon absorption coefficients of proximitized graphene with ferromagnetic exchange coupling $m_F = 0.2$ eV in the absence of intrinsic SOC. In (b)–(d), green, blue and yellow lines correspond to valley $K$, $-K$ and both valleys, respectively. $k_F$ is the Fermi wave vector at valley $K$. Parameters: $\Delta = 0.3$ eV, $\hbar v_F = 6.59$ eV·Å, $E_F = 0.33$ eV, $k_F = 0.061$ Å$^{-1}$, $\lambda_R = 0.225$ eV, $g = 1.5$ eV,[57] $\rho = 3.8 \times 10^{-7}$ kg/m$^2$, $\gamma_0 = \hbar g^2 k_F^4/(16\pi\rho E_F^2) = 1.59 \times 10^7$ s$^{-1}$. Phonon dispersion $\omega = \hbar\bar{c}|\boldsymbol{q}|$, with the average sound velocity $\bar{c} = (c_l + c_t)/2 = 1.66 \times 10^4$ m/s.[57]

The sudden jumps after peaks originate from the dynamical factor $F^{\eta}_{mn}(\boldsymbol{k},\boldsymbol{q})$ in Eq. (3). When $q_x$ becomes larger than $q_{c1}$ or $q_{c2}$, the condition $E_{\eta,n,\boldsymbol{k}-\boldsymbol{q}} = \omega + E_F$ from $F^{\eta}_{mn}(\boldsymbol{k},\boldsymbol{q})$ is no longer satisfied, thus excluding the contribution from valley $K$ or $-K$ and giving rise to the sudden jumps. The results for valley $\pm K$ have the same sign for $\gamma_{D/\bar{D}}$, whereas they have opposite signs for $\gamma_A$. This originates from the opposite Berry curvature of electrons in valley $\pm K$. Since the band dispersion is particle–hole symmetric, we also check the case for the Fermi level lying in the valence band. We find that $\gamma_{D/\bar{D}}$ remains the same, whereas $\gamma_A$ flips the sign. Such behaviors are similar to that of Berry curvature. This suggests that the circular phonon dichroism $\gamma_A$ may provide additional features to reveal the quantum geometric properties of electronic bands.

When the uniform intrinsic SOC is further included, numerical results are plotted in Fig. 2. The Fermi wave vector $k_F$ at valley $K$ becomes larger than valley $-K$. As a result, the transition point $q_{c1}$ ($q_{c2}$) occurs when the contribution from valley $-K$ ($K$) suddenly vanishes. Compared with Fig. 1, a prominent feature in Fig. 2 is that the contribution from valley $-K$ is strongly suppressed at the transition point $q_x = q_{c1}$. Such suppression results from a combination of ferromagnetism, uniform intrinsic and Rashba SOC, which leads to vanishing transition matrix elements between wave vector $\boldsymbol{k}$ and $\boldsymbol{k}-\boldsymbol{q}$, i.e., $[T_x^{\eta=-1}]^{nn}_{\boldsymbol{k},\boldsymbol{k}-\boldsymbol{q}} \approx 0$ and $[T_y^{\eta=-1}]^{nn}_{\boldsymbol{k},\boldsymbol{k}-\boldsymbol{q}} \approx 0$. By contrast, the result for valley $K$ is monotonic and shows sharp peaks at the transition point $q_x = q_{c2}$. The different behaviors at $q_x = q_{c1}$ and $q_{c2}$ originate from the different matrix structures of effective Hamiltonian $H_e(\boldsymbol{k})$ at valleys $K$ and $-K$.

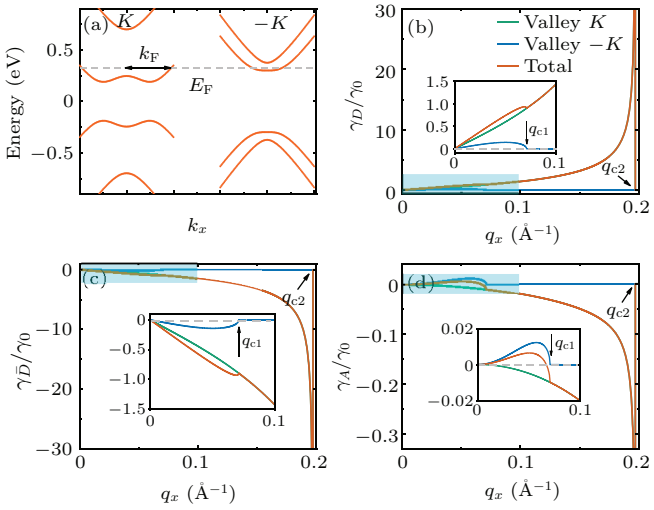



**Fig. 2.** (a) Electronic band structure and (b)–(d) phonon absorption coefficients of proximitized graphene with ferromagnetic exchange coupling $m_F = 0.2$ eV and uniform intrinsic SOC $\lambda_U = 0.2$ eV. Insets of (b)–(d) show the details of the highlighted region. In (b)–(d), green, blue and yellow lines correspond to valley $K$, $-K$ and both valleys, respectively. Parameters: $k_F = 0.096$ Å$^{-1}$, $\gamma_0 = 0.99 \times 10^8$ s$^{-1}$. Other parameters are the same as Fig. 1.

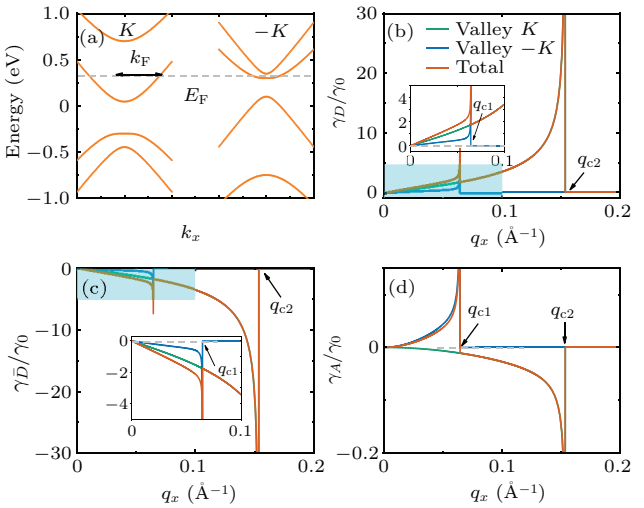



**Fig. 3.** (a) Electronic band structure and (b)–(d) phonon absorption coefficients of proximitized graphene with ferromagnetic exchange coupling $m_F = 0.2$ eV and staggered intrinsic SOC $\lambda_S = 0.2$ eV. Insets of (b) and (c) show the details of the highlighted region. Parameters: $k_F = 0.075$ Å$^{-1}$, $\gamma_0 = 3.7 \times 10^7$ s$^{-1}$. Other parameters are the same as Fig. 1.

When the uniform intrinsic SOC is replaced by the staggered one, numerical results are shown in Fig. 3. We find that $\gamma_{D/\bar{D}/A}$ are strongly enhanced and have peak values at the transition point $q_x = q_{c1}$, in marked contrast to the case with uniform intrinsic SOC. This is because in the presence of staggered SOC, the transition matrix elements $[T_x^{\eta=-1}]^{nn}_{\boldsymbol{k},\boldsymbol{k}-\boldsymbol{q}}$ and $[T_y^{\eta=-1}]^{nn}_{\boldsymbol{k},\boldsymbol{k}-\boldsymbol{q}}$ are nonzero, and the presence of factor $1/\sin\theta$ gives rise to the peak values of $\gamma_{D/\bar{D}/A}$ at the transition point ($\theta \approx 0$). The above studies suggest that in the presence of ferromagnetic exchange coupling, the uniform and staggered intrinsic SOC have distinguishable features in the linear or circular phonon dichroism.

### 3.2. Antiferromagnetic exchange coupling

In this section, we show numerical results of phonon dichroism in graphene with antiferromagnetic exchange coupling ($m_A \neq 0$). When both uniform intrinsic and Rashba SOC are taken into account, numerical results are plotted in Fig. 4. We find that at the transition point $q_x = q_{c1}$ and for valley $-K$, $\gamma_{D/\bar{D}}$ have significant peaks while $\gamma_A$ is strongly suppressed and exhibits non-monotonic behaviors when increasing $q_x$. The difference between $\gamma_{D/\bar{D}}$ and $\gamma_A$ originates from the finite transition $[T_y^{\eta=-1}]^{nn}_{\boldsymbol{k},\boldsymbol{k}-\boldsymbol{q}}$ and vanishingly small transition $[T_x^{\eta=-1}]^{nn}_{\boldsymbol{k},\boldsymbol{k}-\boldsymbol{q}}$. Note that there is a correspondence between AFM with uniform intrinsic SOC and ferromagnetism with staggered intrinsic SOC at valley $K$, thus they have the same $\gamma_{D/\bar{D}/A}$ for valley $K$ as shown in Figs. 3 and 4 (denoted by green curves). Nevertheless, such correspondence fails for valley $-K$, which gives rise to the distinction between the two situations.

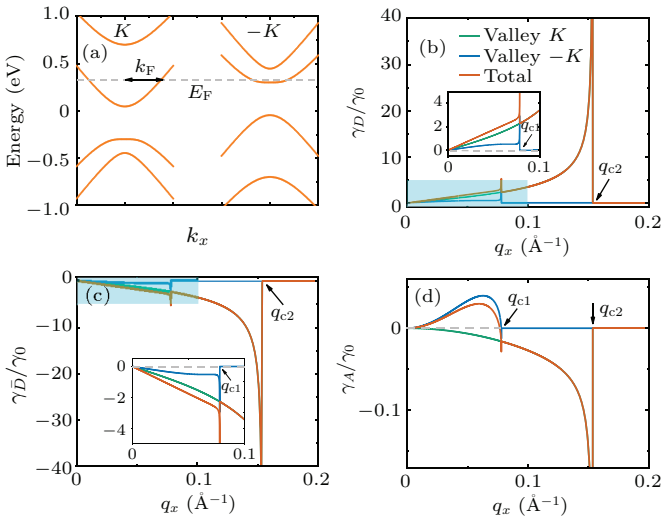



**Fig. 4.** (a) Electronic band structure and (b)–(d) phonon absorption coefficients of proximitized graphene with AFM exchange coupling $m_A = 0.2$ eV and uniform intrinsic SOC $\lambda_U = 0.2$ eV. Insets of (b) and (c) show the details of the highlighted region. Parameters: $k_F = 0.075$ Å$^{-1}$, $\gamma_0 = 3.7 \times 10^7$ s$^{-1}$. Other parameters are the same as Fig. 1.

When the uniform intrinsic SOC is replaced by the staggered one, numerical results are given in Fig. 5. At the transition point $q_x = q_{c1}$ and for valley $-K$, $\gamma_{D/\bar{D}/A}$ are again strongly suppressed. This is due to the fact that $[T_x^{\eta=-1}]^{nn}_{\boldsymbol{k},\boldsymbol{k}-\boldsymbol{q}} \approx 0$ and $[T_y^{\eta=-1}]^{nn}_{\boldsymbol{k},\boldsymbol{k}-\boldsymbol{q}} \approx 0$ at the transition point. Such behaviors are quite similar to the situation with ferromagnetic exchange coupling and uniform intrinsic SOC as in Fig. 2. The reason is that there is a correspondence between AFM with staggered intrinsic SOC and ferromagnetism with uniform intrinsic SOC at valley $-K$. As a result, $\gamma_{D/\bar{D}/A}$ for valley $-K$ are exactly the same between the two situations as shown in Figs. 2 and 5 (denoted by blue curves). However, there is a major difference in the behavior of $\gamma_A$. In Fig. 2(d), $\gamma_A$ for valleys $K$ and $-K$ has opposite signs, therefore the total $\gamma_A$ exhibits a sign change by increasing $q_x$. By contrast, in Fig. 5(d), $\gamma_A$ for valleys $K$ and $-K$ has the same sign, thus the total $\gamma_A$ displays no sign change. This provides the distinguishable features from all above situations.

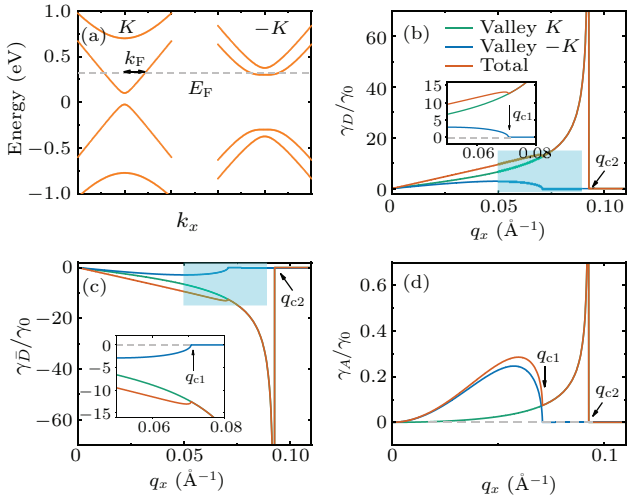



**Fig. 5.** (a) Electronic band structure and (b)–(d) phonon absorption coefficients of proximitized graphene with AFM exchange coupling $m_A = 0.2$ eV and staggered intrinsic SOC $\lambda_S = 0.2$ eV. Insets of (b) and (c) show the details of the highlighted region. Parameters: $k_F = 0.045$ Å$^{-1}$, $\gamma_0 = 0.5 \times 10^7$ s$^{-1}$. Other parameters are the same as Fig. 1.

## 4. Conclusions

To summarize, we systematically study the phonon dichroism in proximitized graphene with external magnetization. We find that any combination of uniform (staggered) intrinsic SOC and ferromagnetic (antiferromagnetic) exchange coupling can lead to nonvanishing phonon dichroism. Qualitatively different behaviors of linear and circular phonon dichroism among these situations are compared, particularly at the transition point. This provides opportunities to apply phonon dichroism effect to detect the form of SOC and magnetic exchange coupling in proximitized graphene.

Note that phonon dichroism has no direct relation to the topological properties of the graphene system. Actually, the situation in Figs. 2, 3, 4 and 5 corresponds to Chern phase with Chern number $C = 2$, metallic phase, Chern phase with $C = 1$ and metallic phase, respectively.[23] Phonon dichroism is more

likely a band geometric quantity, which connects electronic states with wave vectors $\boldsymbol{k}$ and $\boldsymbol{k}-\boldsymbol{q}$. In the long-wavelength limit $\boldsymbol{q}\to 0$, circular phonon dichroism $\gamma_A$ is related to the interband Berry connection.[62] That is the reason why $\gamma_A$ reverses the sign when the Fermi level is tuned from the conduction to valence band in Fig. 1.

In contrast to Weyl semimetals,[52] phonon dichroism in graphene has several distinct features. First, circularly polarized phonons are constructed by non-degenerate longitudinal and transverse acoustic modes in graphene, rather than two degenerate transverse modes in Weyl semimetals. Such non-degeneracy substantially suppresses the out-of-plane phonon angular momentum and the screening effect of electrons.[52,63] Second, the absorption of phonons is much stronger in graphene due to the smaller 2D mass density and larger electron–phonon coupling strength. This suggests that the experimental observation of circular phonon dichroism is more feasible in graphene.

Phonon absorption is qualitatively different from photon absorption. For photon absorption, transitions of electrons are allowed between conduction and valence bands, therefore the optical conductivity is contributed by the band geometric quantities of both conduction and valence bands. For absorption of acoustic phonons, transitions of electrons are within valence (conduction) bands with different wave vectors since acoustic phonon modes are unable to induce the interband transitions. As a result, phonon absorption coefficients depend on the information of band geometries of purely valence (conduction) bands.

The proposed CPD effect can be detected by the pulse-echo technique[64,65] based on different absorption coefficients between left- and right-handed circularly polarized phonons. An alternative detection is the Raman spectroscopy analysis[66,67] of phonon polarization by injecting linearly polarized acoustic waves.

## Appendix A: Numerical method

To numerically calculate the absorption coefficients $\gamma_{D/\bar{D}/A/\bar{A}}$, we can change the integral variable from $\boldsymbol{k}$ to $k=|\boldsymbol{k}|$, $k'=|\boldsymbol{k}-\boldsymbol{q}|$,[53] and obtain

$$\begin{aligned}&\gamma_l(\boldsymbol{q},\omega)\\&=\frac{\hbar}{8\pi\rho\omega}\sum_{n,\eta}\int_0^{\infty}k\,\mathrm{d}k\int_{|k-q|}^{k+q}k'\,\mathrm{d}k'\frac{F^{\eta}_{nn}(\boldsymbol{k},\boldsymbol{q})X_lY}{2qk\sin\theta},\end{aligned}\tag{A1}$$

$l=D,\bar{D},A,\bar{A}$, where

$$\begin{aligned}X_D&=[T_x^{\eta}]^{nn}_{\boldsymbol{k},\boldsymbol{k}-\boldsymbol{q}}[[T_x^{\eta}]^{nn}_{\boldsymbol{k},\boldsymbol{k}-\boldsymbol{q}}]^*+[T_y^{\eta}]^{nn}_{\boldsymbol{k},\boldsymbol{k}-\boldsymbol{q}}[[T_y^{\eta}]^{nn}_{\boldsymbol{k},\boldsymbol{k}-\boldsymbol{q}}]^*,\\X_{\bar{D}}&=[T_x^{\eta}]^{nn}_{\boldsymbol{k},\boldsymbol{k}-\boldsymbol{q}}[[T_x^{\eta}]^{nn}_{\boldsymbol{k},\boldsymbol{k}-\boldsymbol{q}}]^*-[T_y^{\eta}]^{nn}_{\boldsymbol{k},\boldsymbol{k}-\boldsymbol{q}}[[T_y^{\eta}]^{nn}_{\boldsymbol{k},\boldsymbol{k}-\boldsymbol{q}}]^*,\\X_A&=2\mathrm{Im}\{[T_x^{\eta}]^{nn}_{\boldsymbol{k},\boldsymbol{k}-\boldsymbol{q}}[[T_y^{\eta}]^{nn}_{\boldsymbol{k},\boldsymbol{k}-\boldsymbol{q}}]^*\},\\X_{\bar{A}}&=2\mathrm{Re}\{[T_x^{\eta}]^{nn}_{\boldsymbol{k},\boldsymbol{k}-\boldsymbol{q}}[[T_y^{\eta}]^{nn}_{\boldsymbol{k},\boldsymbol{k}-\boldsymbol{q}}]^*\},\end{aligned}\tag{A2}$$

and $Y=\delta_{\phi_{\boldsymbol{k}}=\phi_{\boldsymbol{q}}+\theta}+\delta_{\phi_{\boldsymbol{k}}=\phi_{\boldsymbol{q}}-\theta}$. $\phi_{\boldsymbol{k}}=\tan^{-1}(k_y/k_x)$ and $\phi_{\boldsymbol{q}}=\tan^{-1}(q_y/q_x)$. $\theta$ is the angle between $\boldsymbol{q}$ and $\boldsymbol{k}$, satisfying

$$\begin{aligned}\cos\theta&=\frac{q^2+k^2-k'^2}{2qk},\\\sin\theta&=\frac{\sqrt{4q^2k^2-(q^2+k^2-k'^2)^2}}{2qk}.\end{aligned}\tag{A3}$$

By integrating out the delta function, we have

$$\begin{aligned}\gamma_l(\boldsymbol{q},\omega)=\frac{\hbar}{8\pi\rho}\sum_{n,\eta}&\frac{k}{|\frac{\mathrm{d}E_{\eta,n,k}}{\mathrm{d}k}|}\frac{k'}{|\frac{\mathrm{d}E_{\eta,n,k'}}{\mathrm{d}k'}|}\frac{X_lY}{2qk\sin\theta}\\&\times\delta_{E_{\eta,n,k}=E_{\mathrm{F}}}\delta_{E_{\eta,n,k'}=E_{\mathrm{F}}+\omega}\Theta(k'-|k-q|)\\&\times\Theta(k+q-k').\end{aligned}\tag{A4}$$

$E_{\eta,m,k/k'}$ is eigen-dispersion of electronic Hamiltonian $H_{\mathrm{e}}(\boldsymbol{k})$. $\Theta(\cdot)$ is the Heaviside function. The derivatives can be evaluated numerically by

$$\begin{aligned}\frac{\mathrm{d}E_{\eta,n,k}}{\mathrm{d}k}\delta_{\phi_{\boldsymbol{k}}=\phi_{\boldsymbol{q}}\pm\theta}&=\langle\eta,n,\boldsymbol{k}|\frac{\mathrm{d}H_{\mathrm{e}}(\boldsymbol{k})}{\mathrm{d}k}|\eta,n,\boldsymbol{k}\rangle\delta_{\phi_{\boldsymbol{k}}=\phi_{\boldsymbol{q}}\pm\theta},\\\frac{\mathrm{d}E_{\eta,n,k}}{\mathrm{d}k'}\delta_{\phi_{\boldsymbol{k}}=\phi_{\boldsymbol{q}}\pm\theta}&=\langle\eta,n,\boldsymbol{k}|\frac{\mathrm{d}H_{\mathrm{e}}(\boldsymbol{k}')}{\mathrm{d}k'}|\eta,n,\boldsymbol{k}\rangle\delta_{\phi_{\boldsymbol{k}}=\phi_{\boldsymbol{q}}\pm\theta},\end{aligned}\tag{A5}$$

where

$$\begin{aligned}\frac{\mathrm{d}H_{\mathrm{e}}(\boldsymbol{k})}{\mathrm{d}k}\delta_{\phi_{\boldsymbol{k}}=\phi_{\boldsymbol{q}}\pm\theta}&=\begin{pmatrix}0&f_{\pm}&0&0\\f_{\pm}^*&0&0&0\\0&0&0&f_{\pm}\\0&0&f_{\pm}^*&0\end{pmatrix},\\\frac{\mathrm{d}H_{\mathrm{e}}(\boldsymbol{k}')}{\mathrm{d}k'}\delta_{\phi_{\boldsymbol{k}}=\phi_{\boldsymbol{q}}\pm\theta}&=\begin{pmatrix}0&g_{\pm}&0&0\\g_{\pm}^*&0&0&0\\0&0&0&g_{\pm}\\0&0&g_{\pm}^*&0\end{pmatrix},\end{aligned}\tag{A6}$$

with

$$\begin{aligned}f_{\pm}&=\hbar v_{\mathrm{F}}\,\mathrm{e}^{-\mathrm{i}(\phi_{\boldsymbol{q}}\pm\theta)}\left[1\pm\mathrm{i}\frac{k^2-q^2+k'^2}{2qk\sin\theta}\right],\\g_{\pm}&=\mp\mathrm{i}\hbar v_{\mathrm{F}}\,\mathrm{e}^{-\mathrm{i}(\phi_{\boldsymbol{q}}\pm\theta)}\frac{k'}{q\sin\theta}.\end{aligned}\tag{A7}$$

## Acknowledgements

I am grateful to Yurong Weng for many valuable discussions and comments. This work is supported by the National Natural Science Foundation of China (Grant No. 11904062), the Starting Research Fund from Guangzhou University (Grant No. RQ2020076), and Guangzhou Basic Research Program, jointed funded by Guangzhou University (Grant No. 202201020186).

## References

[1] Ren Y, Qiao Z and Niu Q 2016 *Rep. Prog. Phys.* **79** 066501
[2] Haldane F D M 1988 *Phys. Rev. Lett.* **61** 2015
[3] Kane C L and Mele E J 2005 *Phys. Rev. Lett.* **95** 146802
[4] Kane C L and Mele E J 2005 *Phys. Rev. Lett.* **95** 226801

[5] Yao Y, Ye F, Qi X L, Zhang S C and Fang Z 2007 *Phys. Rev. B* **75** 041401
[6] Gmitra M, Konschuh S, Ertler C, Ambrosch-Draxl C and Fabian J 2009 *Phys. Rev. B* **80** 235431
[7] Gmitra M and Fabian J 2015 *Phys. Rev. B* **92** 155403
[8] Gmitra M, Kochan D, Högl P and Fabian J 2016 *Phys. Rev. B* **93** 155104
[9] Wang Z, Ki D K, Chen H, Berger H, MacDonald A H and Morpurgo A F 2015 *Nat. Commun.* **6** 8339
[10] Yang B, Tu M F, Kim J, Wu Y, Wang H, Alicea J, Wu R, Bockrath M and Shi J 2016 *2D Mater.* **3** 031012
[11] Wang Z, Ki D K, Khoo J Y, Mauro D, Berger H, Levitov L S and Morpurgo A F 2016 *Phys. Rev. X* **6** 041020
[12] Völkl T, Rockinger T, Drienovsky M, Watanabe K, Taniguchi T, Weiss D and Eroms J 2017 *Phys. Rev. B* **96** 125405
[13] Avsar A, Tan J Y, Taychatanapat T, Balakrishnan J, Koon G K W, Yeo Y, Lahiri J, Carvalho A, Rodin A S, O'Farrell E C T, Eda G, Castro Neto A H and Özyilmaz B 2014 *Nat. Commun.* **5** 4875
[14] Omar S and van Wees B J 2017 *Phys. Rev. B* **95** 081404
[15] Dankert A and Dash S P 2017 *Nat. Commun.* **8** 16093
[16] Offidani M, Milletarì M, Raimondi R and Ferreira A 2017 *Phys. Rev. Lett.* **119** 196801
[17] Kaloni T P, Kou L, Frauenheim T and Schwingenschlögl U 2014 *Appl. Phys. Lett.* **105** 233112
[18] Zihlmann S, Cummings A W, Garcia J H, Kedves M, Watanabe K, Taniguchi T, Schönenberger C and Makk P 2018 *Phys. Rev. B* **97** 075434
[19] Ghiasi T S, Ingla-Aynés J, Kaverzin A A and van Wees B J 2017 *Nano Lett.* **17** 7528
[20] Cummings A W, Garcia J H, Fabian J and Roche S 2017 *Phys. Rev. Lett.* **119** 206601
[21] Benítez L A, Sierra J F, Torres W S, Arrighi A, Bonell F, Costache M V and Valenzuela S O 2018 *Nat. Phys.* **14** 303
[22] Frank T, Högl P, Gmitra M, Kochan D and Fabian J 2018 *Phys. Rev. Lett.* **120** 156402
[23] Högl P, Frank T, Zollner K, Kochan D, Gmitra M and Fabian J 2020 *Phys. Rev. Lett.* **124** 136403
[24] Qiao Z, Yang S A, Feng W, Tse W K, Ding J, Yao Y, Wang J and Niu Q 2010 *Phys. Rev. B* **82** 161414
[25] Zollner K, Gmitra M, Frank T and Fabian J 2016 *Phys. Rev. B* **94** 155441
[26] Lazić P, Belashchenko K D and Žutić I 2016 *Phys. Rev. B* **93** 241401
[27] Wang Z, Tang C, Sachs R, Barlas Y and Shi J 2015 *Phys. Rev. Lett.* **114** 016603
[28] Leutenantsmeyer J C, Kaverzin A A, Wojtaszek M and van Wees B J 2017 *2D Mater.* **4** 014001
[29] Mendes J B S, Alves Santos O, Meireles L M, Lacerda R G, Vilela-Leão L H, Machado F L A, Rodríguez-Suárez R L, Azevedo A and Rezende S M 2015 *Phys. Rev. Lett.* **115** 226601
[30] Swartz A G, Odenthal P M, Hao Y, Ruoff R S and Kawakami R K 2012 *ACS Nano* **6** 10063
[31] Wei P, Lee S, Lemaitre F, Pinel L, Cutaia D, Cha W, Katmis F, Zhu Y, Heiman D, Hone J, Moodera J S and Chen C T 2016 *Nat. Mater.* **15** 711
[32] Haugen H, Huertas-Hernando D and Brataas A 2008 *Phys. Rev. B* **77** 115406
[33] Yang H X, Hallal A, Terrade D, Waintal X, Roche S and Chshiev M 2013 *Phys. Rev. Lett.* **110** 046603
[34] Hallal A, Ibrahim F, Yang H, Roche S and Chshiev M 2017 *2D Mater.* **4** 025074
[35] Dyrdal A and Barnaś J 2017 *2D Mater.* **4** 034003
[36] Zollner K, Gmitra M and Fabian J 2018 *New J. Phys.* **20** 073007
[37] Zhang J, Zhao B, Zhou T, Xue Y, Ma C and Yang Z 2018 *Phys. Rev. B* **97** 085401
[38] Qiao Z, Ren W, Chen H, Bellaiche L, Zhang Z, MacDonald A H and Niu Q 2014 *Phys. Rev. Lett.* **112** 116404
[39] Li X, Cao T, Niu Q, Shi J and Feng J 2013 *Proc. Natl. Acad. Sci. USA* **110** 3738
[40] Pei Q, Wang X C, Zou J J and Mi W B 2018 *Front. Phys.* **13** 137105
[41] Zollner K and Fabian J 2022 *Phys. Rev. B* **106** 035137
[42] Wiedenmann A, Rossat-Mignod J, Louisy A, Brec R and Rouxel J 1981 *Solid State Commun.* **40** 1067
[43] Sivadas N, Daniels M W, Swendsen R H, Okamoto S and Xiao D 2015 *Phys. Rev. B* **91** 235425
[44] Barkeshli M, Chung S B and Qi X L 2012 *Phys. Rev. B* **85** 245107
[45] Hamada M, Minamitani E, Hirayama M and Murakami S 2018 *Phys. Rev. Lett.* **121** 175301
[46] Cheng B, Schumann T, Wang Y, Zhang X, Barbalas D, Stemmer S and Armitage N P 2020 *Nano Lett.* **20** 5991
[47] Ren Y, Xiao C, Saparov D and Niu Q 2021 *Phys. Rev. Lett.* **127** 186403
[48] Baydin A, Hernandez F G G, Rodriguez-Vega M, Okazaki A K, Tay F, Noe G T, Katayama I, Takeda J, Nojiri H, Rappl P H O, Abramof E, Fiete G A and Kono J 2022 *Phys. Rev. Lett.* **128** 075901
[49] Xiong G, Chen H, Ma D and Zhang L 2022 *Phys. Rev. B* **106** 144302
[50] Spivak B Z and Andreev A V 2016 *Phys. Rev. B* **93** 085107
[51] Sengupta S, Lhachemi M N Y and Garate I 2020 *Phys. Rev. Lett.* **125** 146402
[52] Liu D and Shi J 2017 *Phys. Rev. Lett.* **119** 075301
[53] Shan W Y 2022 *Phys. Rev. B* **105** L121302
[54] Gmitra M, Kochan D and Fabian J 2013 *Phys. Rev. Lett.* **110** 246602
[55] Kochan D, Irmer S and Fabian J 2017 *Phys. Rev. B* **95** 165415
[56] Shan W Y 2020 *Phys. Rev. B* **102** 241301
[57] Suzuura H and Ando T 2002 *Phys. Rev. B* **65** 235412
[58] Mariani E and von Oppen F 2008 *Phys. Rev. Lett.* **100** 076801
[59] Castro E V, Ochoa H, Katsnelson M I, Gorbachev R V, Elias D C, Novoselov K S, Geim A K and Guinea F 2010 *Phys. Rev. Lett.* **105** 266601
[60] Mariani E and von Oppen F 2010 *Phys. Rev. B* **82** 195403
[61] Amorim B and Guinea F 2013 *Phys. Rev. B* **88** 115418
[62] Shan W Y 2023 *Phys. Rev. Res.* **5** L022038
[63] Tuegel T I and Hughes T L 2017 *Phys. Rev. B* **96** 174524
[64] Truell R, Elbaum C and Chick B B 1969 *Ultrasonic Methods in Solid State Physics* (New York: Academic Press) p. 53
[65] Lüthi B 2004 *Physical Acoustics in the Solid State* 1st edn. (Berlin Heidelberg: Springer) p. 17
[66] Sonntag J, Reichardt S, Beschoten B and Stampfer C 2021 *Nano Lett.* **21** 2898
[67] Kossacki P, Faugeras C, Kühne M, Orlita M, Mahmood A, Dujardin E, Nair R R, Geim A K and Potemski M 2012 *Phys. Rev. B* **86** 205431